

Moisture-based green energy harvesting over 600 hours via photocatalysis-enhanced hydrovoltaic effect

Received: 14 June 2024

Accepted: 11 December 2024

Published online: 02 January 2025



Peng Duan¹, Chenxing Wang¹, Yinpeng Huang¹, Chunqiao Fu¹, Xulei Lu¹, Yong Zhang¹, Yuming Yao¹, Lei Chen¹, Qi-Chang He^{1,2}, Linmao Qian¹ & Tingting Yang^{1,3} ✉

Harvesting the energy from the interaction between hygroscopic materials and atmospheric water can generate green and clean energy. However, the ion diffusion process of moisture-induced dissociation leads to the disappearance of the ion concentration gradient gradually, and there is still a lack of moisture-based power generation devices with truly continuous operation, especially the duration of the current output still needs to be extended. Here, we propose a design for reconstructing the ion concentration gradient by coupling photocatalytic hydrogen evolution reaction with hydrovoltaic effect, to report a moisture-enabled electric generator (MEG) with continuous current output. We show that the introduction of the photocatalytic layer not only absorbs light energy to greatly increase the power generation of the MEG (500% power density enhancement), but more importantly, the photocatalytic hydrogen evolution process consumes the pre-stacked ions to restore the ion concentration gradient, allowing the MEG to continuously output current for more than 600 hours, which is 1 to 2 orders of magnitude higher than the great majority of existed MEGs in terms of the current output duration.

Moisture-enabled electric generator (MEG) technology directly converts the energy stored in the gas-liquid phase change process of moisture into electrical energy^{1–4}. This emerging technology has the advantages of being green, clean and having a wide coverage area, and can complement existing environmental energy harvesting technologies^{5–9}. Output power density and lifespan are two key indicators for measuring the performance of MEG, which directly determine the possible application direction of the device. After nearly 10 years of development, moisture-enabled electric materials with rich surface states and excellent ion transport properties and device structures that reduce energy dissipation have significantly enhanced power density. The power density of MEGs based on the pure hydrovoltaic effect has increased from the initial 18.4 nW/cm² to 12 μW/cm² in recent years^{10–12}. Compared with the widely studied power density,

lifespan is an indicator that receives less attention. Many existing MEGs have a short power generation time (seconds to hours) and are disposable, which greatly hinders the large-scale deployment and application of MEGs^{13–18}.

Power generation mainly depends on the generation, separation, and transmission of carriers (especially ions). To extend the power output time of MEG, continuous moisture absorption-desorption and maintenance of ion concentration gradient are particularly important. Current efforts to improve lifespan include the development of new materials (protein nanowires^{19,20}, graphene oxide^{21–23}, conductive polymer^{24,25}, cellulose^{26–28}) to form nanopores inside the device while ensuring better hydrophilicity, as well as the development of new structures (PN junctions^{29–33}, antisymmetric moisture absorption-desorption^{34–36}, etc.) to provide a gradient for ion transport.

¹Tribology Research Institute, School of Mechanical Engineering, Southwest Jiaotong University, Chengdu 610031, PR China. ²MSME, Université Gustave Eiffel, CNRS UMR 8208, F-77454 Marne-la-Vallée, France. ³Institute of Smart City and Intelligent Transportation, Southwest Jiaotong University, Chengdu 611756, PR China. ✉e-mail: yangtingting@swjtu.edu.cn

Asymmetric structures can create stronger concentration gradients and enhance the directional migration of ions. Combining the two can achieve a benign coupling of material hygroscopicity and gradient maintenance^{11,37–42}, realize continuous ion migration inside the device, and thus extend the electrical output of the device. On this basis, significant progress has been made in the continuous output voltage time of devices in humid environments. For example, the power generation voltages of 0.5 V, 0.6 V, and 1.1 V can be maintained for 1500 h¹⁹, 120 h³⁷, and 258 h³⁸, respectively. Current and voltage are the two most intuitive parameters that characterize the electrical output performance of MEG devices, which are affected by factors such as the properties of ions, the movement speed of ions, and the wetting behavior of the material³⁹. In addition, the number of ion transfers, diffusion coefficients, and concentration gradients in the nanopores will also affect the electric output. Among them, the transport speed and migration amount of ions are closely related to the current output of MEG, and the separation degree of ions on both sides of the electrodes is closely related to the voltage output of MEG. Due to the essential difference between the two, although the initial ion concentration gradient drives the ion diffusion, the migration of the preceding ions will produce a reverse built-in potential and weaken the ion concentration gradient. Insufficiently motivated migration of the subsequent ions results in a device that still outputs voltage but not current. Thus, the current of the above devices can only be maintained for 20 h¹⁹, 12 h³⁷, and 150 h³⁸. Therefore, it is crucial to innovate ion transport regulation strategies to maintain the ion migration dynamics and improve the current output duration of the MEG.

Our previous work utilized the redox reaction of the metal electrode to consume the pre-stacked ions and clear the way for the continuous migration of subsequent ions. The current output duration of the device was improved to 1 month⁴⁰. In the work published so far, some devices have achieved electrical output for more than 1 month. However, redox reactions⁴⁰ or moisture absorption-dehumidification cycles that depend on humidity changes^{11,19} will limit the application of MEGs. In addition, Tao et al. combined rapid moisture absorption with slow movement of water clusters to provide a new idea for long-term power generation¹. Guo et al. combined hygroscopicity and evaporation to achieve water circulation inside the device¹⁵. However, these devices will inevitably fail to continuously generate electrical output due to the gradual disappearance of the ion concentration gradient. Introducing green light energy into the device to maintain the redox reaction seems to provide another solution to this problem. Tan et al. innovatively coupled hygroscopic hydrogels with photocatalytic hydrogen production, and developed an atmospheric water-splitting device that can spontaneously absorb moisture, produce hydrogen, and generate electricity under illumination^{41–44}. The above work mainly focuses on how hygroscopic mass transfer facilitates photocatalytic hydrogen production and energy conversion, and has not yet explored the enhancing effect of photocatalysis on the hydrovoltaic process, especially the continuous migration of charge carriers.

In this work, we propose a strategy to use photocatalysis to consume the pre-stacked ions in the device and then rebuild the ion concentration gradient to restore the current output. The device consists of three parts: a hydrogel moisture-enabled electricity generation layer (MEL), a photocatalytic layer (PCL), and inert electrode layers. Under high humidity and no light environment, the hydrovoltaic effect endows the device with moisture-based power generation capability: the output V_{OC} is 0.28 V, and the peak I_{SC} is 1.8 μA . As power generation proceeds, the ion migration momentum decreases and the output current continues to decay. Moderate light stimulation rebuilds the ion concentration gradient inside the device, accompanied by hydrogen generation and light energy conversion for power generation. After the illumination, the device power generation is restored in the pure hydrovoltaic effect mode, and the current output duration can be extended to 650 h. Our work promotes the

understanding of photocatalytically enhanced hydrovoltaic power generation and advances the sustainable green and high-quality development of MEGs.

Results

Design and characterization of the device

The moisture-based power generation process depends on the directional transport of ions in the nanoconfined space. We chose the polyacrylamide/2-acrylamido-2-methylpropane sulfonic acid/lithium chloride (PAM/AMPS/LiCl) hydrogel enriched with a large number of hydrophilic functional groups to construct the MEL (Fig. 1a)⁴⁵. In order to increase the moisture adsorption sites, an appropriate amount of LiCl is added to capture moisture and convert it into liquid water which is stored in the polymer network. Since the upper and lower surfaces of the MEL are asymmetrically exposed to the humid environment, the abundant liquid water near the upper electrode (porous gold) causes a large amount of dissociation of the sulfonic acid groups inside the gel, releasing the negatively charged sulfonic acid groups fixed in the network and the free positively charged hydrogen ions^{24,45} (Supplementary Fig. 1). The asymmetric moisture absorption and dissociation of the MEL leads to an ionic concentration difference inside the device, driving the free ions to move rapidly in the direction of the concentration gradient while triggering charge separation. The spatial separation of positive and negative charges generates the V_{OC} of the device, and the continuous migration of positive and negative charges generates the I_{SC} .

However, after the migration of the preceding hydrogen ions, they will be enriched on the lower surface of the MEL to generate a reverse electric field that hinders the subsequent migration of hydrogen ions, accompanied by a gradual decrease in the ion concentration gradient between the upper and lower sides of the MEL. These two reasons led to a 77.5% decrease in the current output of the device (98% RH, 25 °C) during the 0–448 h period (Fig. 1b). To solve this problem, we added photosensitized carbon nitride (P-CN)/polyvinylidene fluoride-hexafluoropropylene (PVDF-HFP) as a photocatalytic layer between the lower surface of the MEL and the bottom electrode. When illumination is applied (yellow area in Fig. 1b), photogenerated electron-hole separation is generated in the PCL near the lower surface of the MEL. The photogenerated electrons recombine with hydrogen ions to release hydrogen and rebuild the ion concentration gradient inside the MEL. The photogenerated holes are collected by the bottom electrode (carbon nanotubes (CNT)/poly(3,4-ethylenedioxythiophene): poly(styrenesulfonate) (PEDOT: PSS)) to output external current, that is, the hydrovoltaic and photocatalytic effects synergistically generate electricity to enhance the electrical output (500% improvement compared to the pure hydrovoltaic control sample without illumination). After ~4 h of illumination, the photocatalytic hydrogen evolution reaction ends, and the device power generation depends only on the hydrovoltaic effect. Interestingly, the device's current output is 150% higher than before illumination. Moreover, after the photocatalytic reconstruction of the ion concentration gradient, the device power generation is restored, and the current output time can be extended to 650 h, while the voltage can remain stable for a long time (Supplementary Fig. 2). The power generation of our device is higher than that of most previously reported pure hydrovoltaic devices (inactive electrodes, Supplementary Table 1), and the I_{SC} duration far exceeds that of existing power generation devices (Fig. 1c).

In order to investigate the microstructure and physicochemical properties of the device, we characterize different parts of the device. The device is a multilayer stacked structure (Fig. 2a), and the detailed preparation process is shown in the methods section (Supplementary Fig. 3). From top to bottom, the device consists of a porous gold upper electrode (light-transmitting and moisture-permeable), a hygroscopic gel (MEL), a P-CN/PVDF-HFP self-supporting film (PCL), and a CNT/

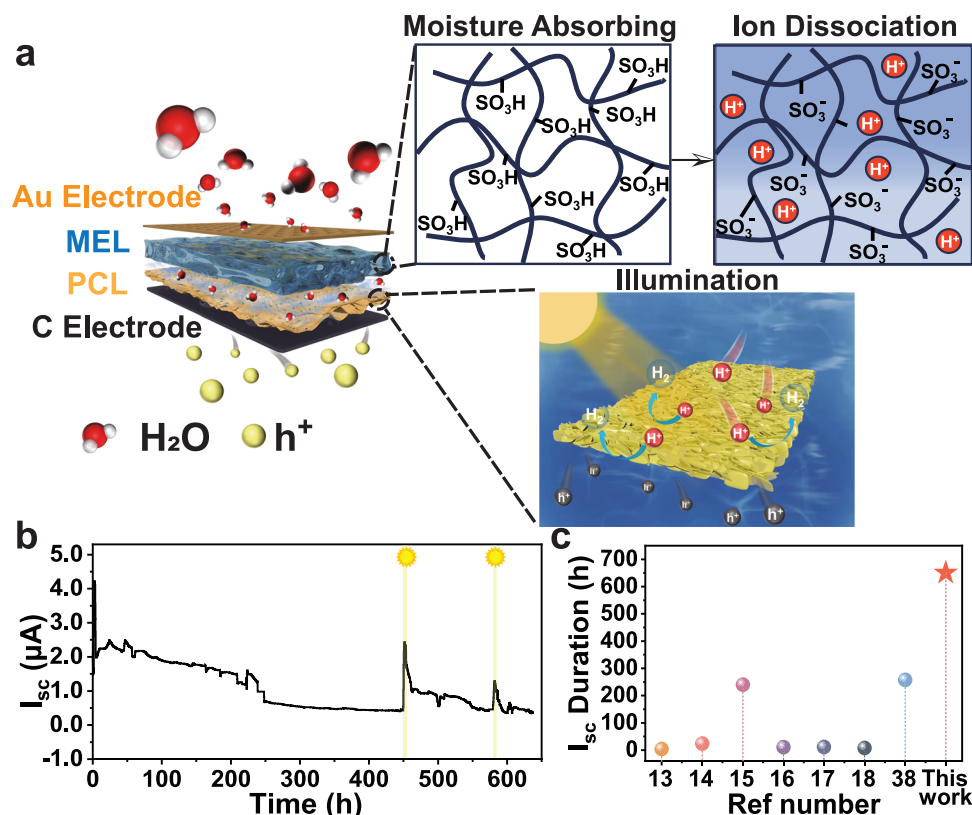


Fig. 1 | Design and performance of our moisture-enabled electric generator (MEG). **a** Schematic diagram of device structure. The moisture-enabled electricity generation layer (MEL) in the device can absorb moisture in the air and dissociate hydrogen ions, and the photocatalytic layer (PCL) below can consume

the hydrogen ions under the action of light. (h⁺ is in reference to holes).

b Schematic diagram of long-time I_{sc} (yellow area is the part of illumination).

c Comparison of I_{sc} duration of published MEGs^{13–18,38}. The source data are available in the “Data availability” section.

PEDOT: PSS bottom electrode (placed on a glass slide, moisture-impermeable). Scanning electron microscope (SEM) images show the skeleton structure of the top and cross-section of the MEL, showing a directional and uniform porous structure, which is conducive to the moisture absorption of the MEL and the rapid transport of ions in the MEL. In addition, the MEL is highly transparent, allowing light to reach the surface of PCL effectively (Supplementary Fig. 4). PVDF-HFP is an effective binder capable of forming a film of P-CN powder into a porous structure, and the P-CN powder is embedded inside the porous structure and on the surface of the film (Fig. 2a and Supplementary Fig. 5). The bottom electrode is sprayed on the other side of the PCL (Fig. 2a). In order to promote stronger light absorption and electron-hole separation, the graphite phase carbon nitride (g-C₃N₄, CN) needs to be impregnated with chlorophyllin sodium copper salt (Chl) to obtain photosensitized carbon nitride (x P-CN) (where the number denotes the concentration of Chl in mg/L). The X-ray diffraction (XRD) images of CN powder before and after modification are shown in Fig. 2b. The two peaks at 2θ values of 12.7° and 27.5° are attributed to (100) and (002) reflections, respectively. The Fourier transform infrared spectroscopy (FTIR) image of the P-CN shows similar peak positions to the CN (Fig. 2c), which basically maintain the chemical structure of the CN. The X-ray photoelectron spectroscopy (XPS) spectra of the P-CN (Fig. 2d, e) show obvious C and N main peaks and other peak positions. The results obtained by the three characterization methods are consistent with the previously reported data^{46,47}.

Mechanism of photocatalytic enhancement on hydrovoltaic performance

Figure 3a illustrates the charge transfer mechanism in P-CN under illumination. The conduction band (CB) and valence band (VB) of CN

are −1.14 eV and 1.6 eV, respectively (Supplementary Fig. 6). When light is irradiated on the surface of P-CN, Chl will be excited by the photon energy to produce e^- and form Chl*. At the same time, e^- will also be excited from the VB to the CB of CN, thereby generating active photogenerated electrons in the CB and photogenerated holes in the VB (Eq. (1)). The electrons generated by Chl are transferred to the CB of CN to saturate the CB of CN⁴⁸. The electrons participate in the reaction of converting H⁺ to hydrogen to consume hydrogen ions (Eq. (2)). At the same time, some electrons and holes react with dissolved oxygen in the solution to generate superoxide radicals and hydroxyl radicals (Eqs. (3) and (4)). The relevant reaction equation is as follows^{49,50}:

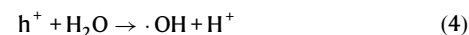
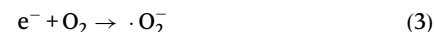
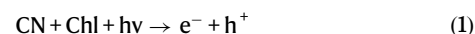


Figure 3b shows a schematic diagram of ions passing through the nanofluidic pores in the PCL. On the one hand, the P-CN/PVDF membrane can be used as a photocatalytic membrane to consume hydrogen ions. On the other hand, the Zeta potential test of the material shows that the Zeta potential of the P-CN is −12.2 mV, simulation (Supplementary Fig. 7) and ion selectivity experiments (Supplementary Fig. 8) show that the nanopore has cation selectivity and promote

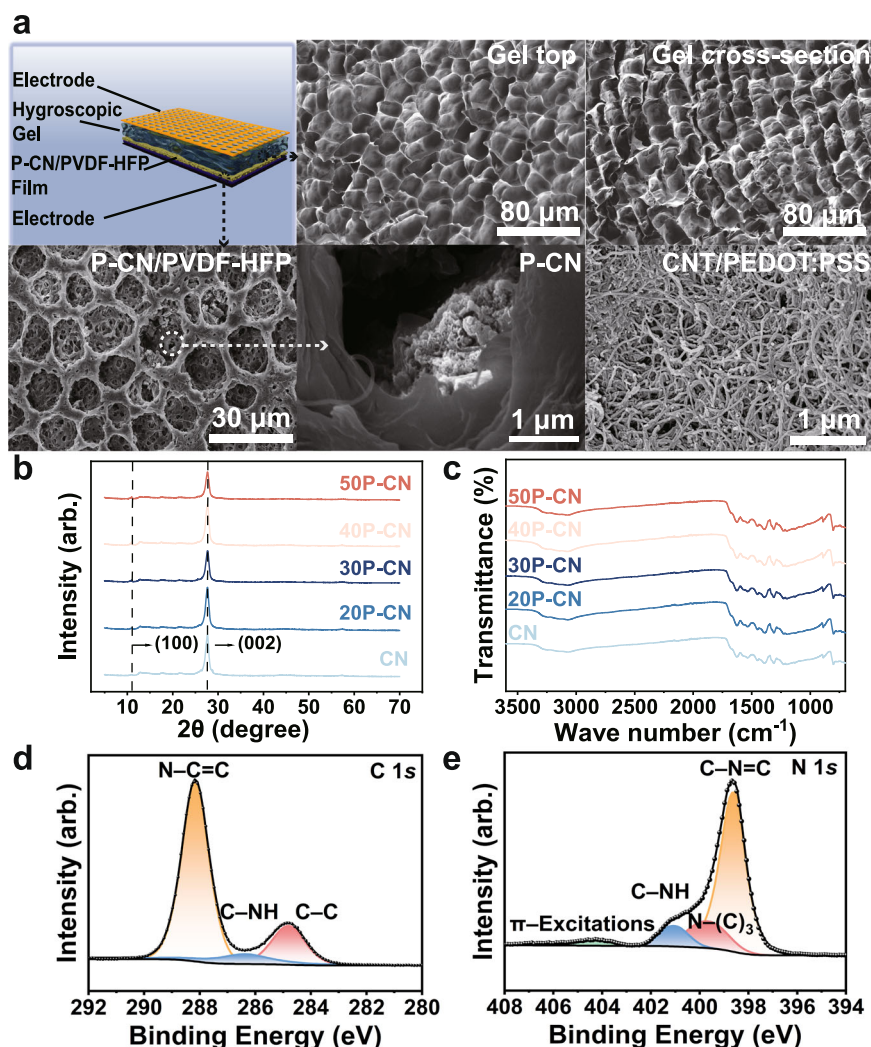


Fig. 2 | Structure and characterization of the device. **a** Schematic diagram of the device structure and SEM spectrums of each part, **b** XRD spectrums of CN and P-CN, **c** FTIR spectrums of CN and P-CN, **d**, **e** XPS spectrums of P-CN. The high-resolution C1s spectrum shows three peaks at 284.8 eV (C-C), 286.36 eV (C-NH),

288.16 eV (N-C=C), and the N1s spectrum shows three peaks at 398.57 eV (C-N=C), 388.62 eV (N-(C)₃), 401.04 eV (C-NH). The source data are available in the “Data availability” section.

the spatial separation of anions and cations. In addition, we conducted an impedance test and the equivalent circuit diagram is shown in the inset of Supplementary Fig. 9. The conductivity of the device can be calculated to be 0.1711 $\mu\text{S}/\text{cm}$ through the equivalent circuit.

Using DMPO (5,5-Dimethyl-1-pyrroline N-oxide) as the capture agent, the substances generated during the photocatalytic process are proved by free radical capture experiments. As can be seen in Fig. 3c, d, after 10 min of irradiation (450 nm light source) of the P-CN, the EPR spectrum shows that the superoxide free radical capture experiment presents 6 characteristic peaks (of which 1, 2, 4, and 6 peaks have high intensity, and 3 and 5 peaks have low intensity), and the hydroxyl free radical capture experiment presents 4 characteristic peaks (intensity ratio is 1:2:2:1), which are consistent with the standard waveform, proving that the photocatalytic reaction generates intermediate substances.

To illustrate the necessity of Chl modification of CN, the optical absorption properties of the photocatalytic materials are determined by using ultraviolet-visible diffuse reflectance spectroscopy (UV-Vis DRS) (Fig. 3e). The P-CN obtained from the modified treatment of CN using Chl shows more intense light absorption in both UV and visible wavelength ranges. The addition of PVDF-HFP has little effect on the light absorption capacity of the composite film. The

Photoluminescence (PL) spectra (excitation wavelength of 380 nm) are used to characterize the electron-hole separation efficiency of the photocatalytic material (Fig. 3f). The spectra shows that the fluorescence emission peak patterns of the CN and the P-CN are relatively consistent, with the shoulder peaks all around 460 nm. Among the P-CN (from 20 to 50 P-CN) obtained by using Chl to modify CN, the peak intensity of 30 P-CN is the lowest, which indicates that this degree of photosensitization treatment can achieve more efficient photo-generated charge separation of the material. The improved electron-hole separation efficiency helps to consume the hydrogen ions enriched at the bottom electrode upon illumination.

The consumption of hydrogen ions near the bottom electrode helps the reconstruction of the ion concentration gradient. Figure 4a clearly shows the processes of generation, decline, and reconstruction of the ion concentration gradient in the MEL. Initially, the hydrogel layer is in a dry state, and the sulfonic acid groups will not dissociate. At this time, the interior of the MEL is in an anhydrous and ion-free state. When the MEL is placed into a humid environment, the asymmetric hygroscopicity of the MEL and the dissociation of the sulfonic acid groups will create the concentration gradients of hydrogen ions and water inside the MEL. The presence of gradient energy drives the ions to migrate directionally in the direction of the concentration gradient

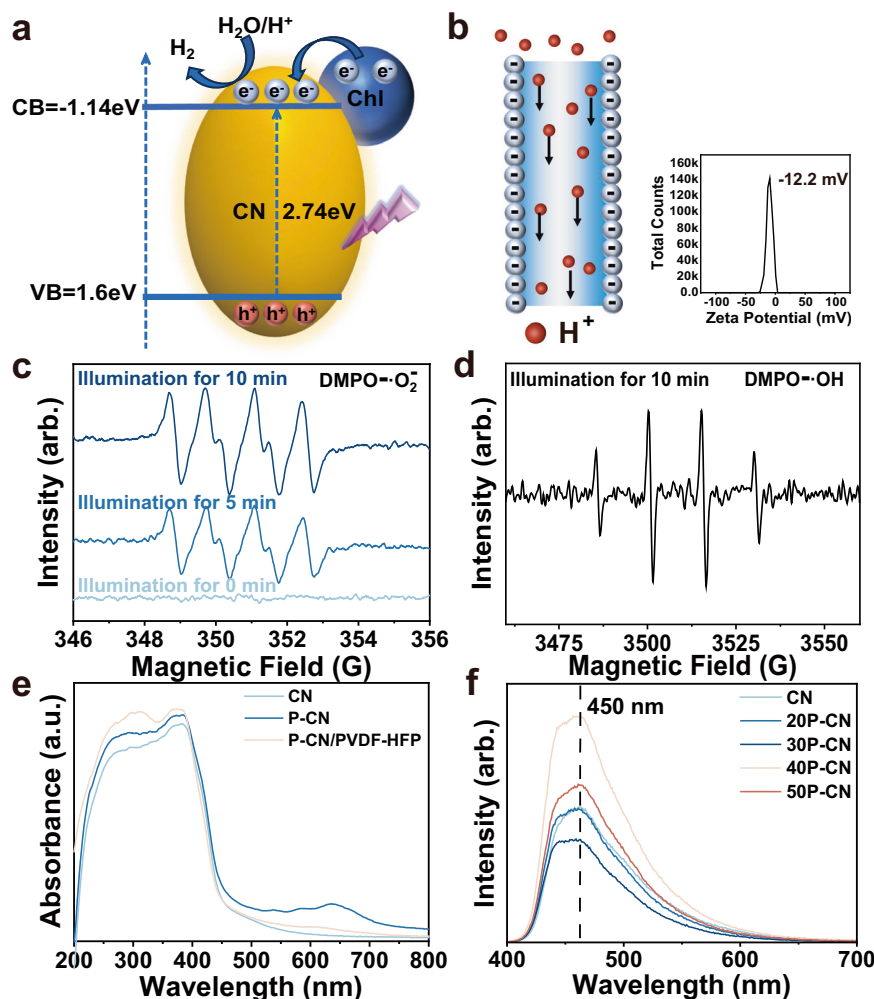


Fig. 3 | Characterization of photocatalytic properties. **a** Band structure of the P-CN. **b** Schematic representation of charge transfer in the internal pores of the PCL. **c, d** Electron paramagnetic resonance (EPR) spectra of superoxide radicals and hydroxyl radicals. **e** Ultraviolet-visible diffuse reflectance spectroscopy (UV-Vis

DRS) spectra of the CN, P-CN and P-CN/PVDF-HFP. **f** Photoluminescence (PL) spectra of the CN and the P-CN with excitation wavelength of 380 nm. The source data are available in the “Data availability” section.

to generate current. As the device saturates with adsorption and the accumulation of preceding ions hinders the diffusion of subsequent ions. The ion distribution stabilizes and the current output is greatly diminished. Subsequently, the device is illuminated, and the photocatalytic effect consumes hydrogen ions near the bottom of the MEL to produce hydrogen overflow. In the test environment (98% RH, 25 °C), the hydrogen production of the device (light-illuminated for 4 h) is measured by the trace gas analysis system to be $\sim 6.77 \mu\text{mol}$ (Supplementary Table 2), and the hydrogen ion concentration gradient within the MEL is reconstructed. After illumination, the ions migrate directionally from the upper region to the lower region again, and the electrical output is greatly restored.

To verify the effect of illumination on the reconstruction of the hydrogen ion concentration gradient in the MEL, the pH values of the upper and lower surfaces of the PCL and the MEL before and after illumination are tested using a planar pH meter (Fig. 4b). Among them, the pH values of the upper and lower surfaces of the PCL increase from ~ -0.6 to ~ 2.4 after illumination, indicating that the hydrogen ions are effectively consumed. The pH values of the upper and lower surfaces of the MEL increase from -0.73 and -0.53 to 1.27 and 1.93 , respectively, after illumination. Before illumination, the pH value difference between the upper and lower surfaces of the MEL is 0.2 , and after illumination, the difference increases to ~ 0.7 , indicating that the ion concentration gradient is effectively rebuilt. In addition, we used

molecular simulation to calculate the hydrogen ion transport before and after the reconstruction of the concentration gradient (Supplementary Fig. 10). In the system without concentration gradient, the density distribution of H_3O^+ did not change significantly. In other words, in the system without concentration gradient, H_3O^+ did not diffuse in a directional manner (Supplementary Fig. 11). In the system with concentration gradient, there was an obvious migration of H_3O^+ from the high concentration side to the low concentration side along the concentration gradient, which is consistent with the experimental results (Supplementary Fig. 12). In addition, the change of H_3O^+ along the z-axis direction also proves that the concentration gradient will act as a power source to drive the transport of H_3O^+ along the concentration gradient direction (Supplementary Fig. 13).

It is worth noting that illumination also leads to the reduction of hydrogen ions on the upper surface of the MEL, which might be a disadvantage for hydrovoltaic power generation, and thus, the optimal illumination time needs to be explored. As shown in Fig. 4c and Supplementary Fig. 14, after a period of pure hydrovoltaic power output, the current output of the three groups of devices decay from the initial current (μA level) to a lower level. The three groups of devices were tested for short (1 h), medium (4 h), and long (8 h) illumination. It's found that after 1 h illumination, the current of the device only recovers to 10% of the initial current data. This may be due to the low consumption of hydrogen ions near the lower surface of the MEL that

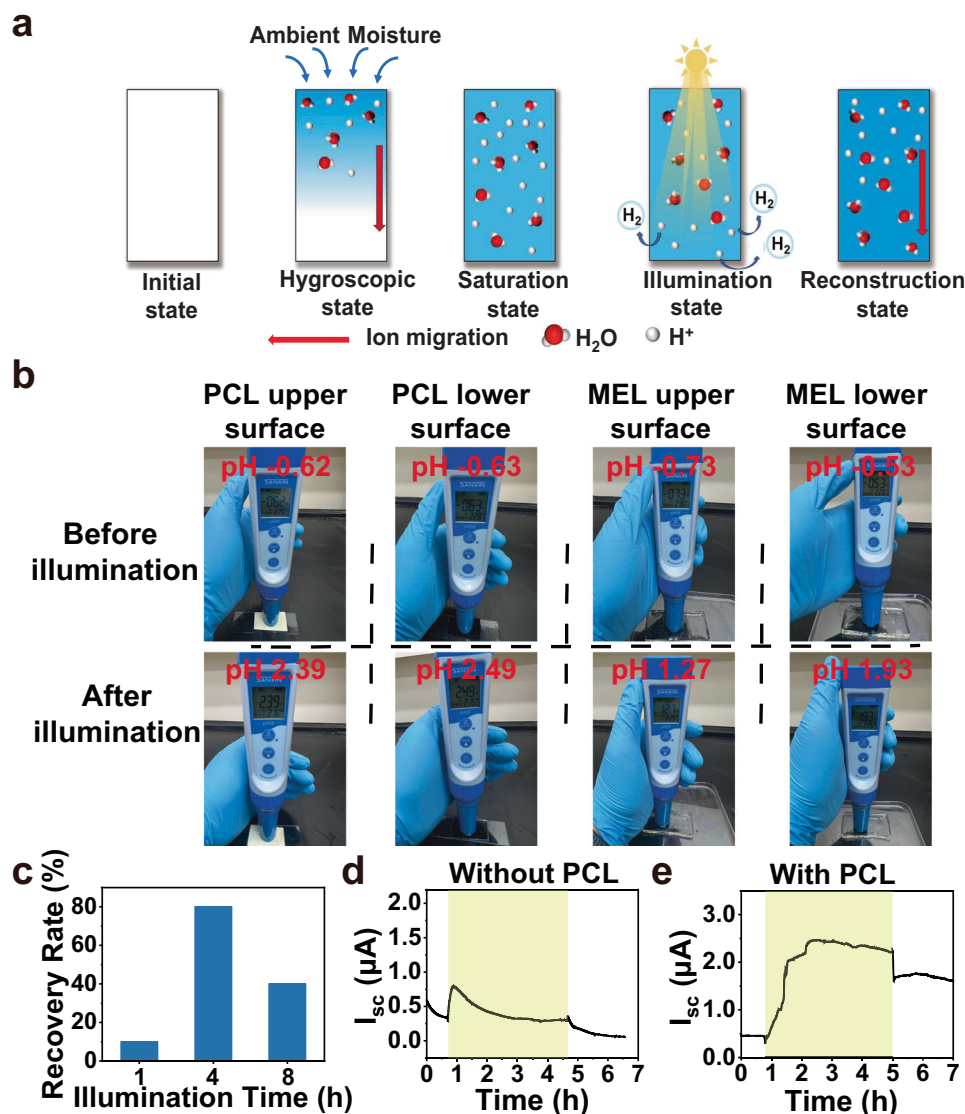


Fig. 4 | Verification of the mechanism of photocatalytic effect to rebuild ion concentration gradient. **a** Schematic diagram of moisture absorption and ion transport inside the MEL. **b** pH value of PCL and MEL surface before and after illumination. **c** Comparison of current recovery effect after illumination for

different periods. **d, e** Effect of the PCL on electrical output recovery (yellow is the part with illumination applied). The source data are available in the "Data availability" section.

fails to rebuild the gradient. The device after 8 h of illumination achieves current recovery, but only to 40% of the initial current output, which may be due to the fact that longer illumination can over-consume hydrogen ions inside the MEL, and the insufficient number of hydrogen ions involved in directional migration leads to lower current levels. The optimal illumination time is 4 h, at which time the current recovery value reaches ~80%. To further illustrate the importance of PCL and exclude the role of thermal effects, we set up control experiments with and without PCL (Fig. 4d, e). In a humid environment (98%, 25 °C), the current output of the two groups of hydrovoltaic devices initially decays to a low level, and the same light source is used to illuminate the two groups of devices (450 nm LED light source, 1.5 A, 4 h). After illumination, the current of the experimental group with the PCL recovers effectively, while the control group without the PCL fails to achieve effective recovery. This indicates that the reconstruction of the ion concentration gradient is due to photocatalysis rather than photothermal effect. In summary, the photocatalytic enhancement of the life of hydrovoltaic devices originates from the photocatalytic-assisted reconstruction of ion concentration gradient.

Performance influencing factors and application prospects

The directional transport of ions is closely related to the physico-chemical properties of nanochannels. Therefore, it is necessary to investigate the composition and microstructure control methods of MEL and PCL to obtain the optimal process parameters to improve the device performance. Figure 5a shows the effect of the composition ratio of P-CN to PVDF-HFP on the performance of hydrovoltaic power generation. When the P-CN content is relatively small, the PVDF-HFP membrane surface is weakly charged and the pores are large, and the weakened Debye screening effect is not conducive to the spatial separation of anions and cations, resulting in poor electrical output performance. When there are relatively few PVDF-HFP, the P-CN particles are difficult to effectively connect to form a self-supporting film, and the excessive agglomeration of particles and pore collapse will also weaken the electrical output. Therefore, the optimal composition ratio of P-CN to PVDF-HFP is 1:1. MEL is the energy source for hydrovoltaic power generation, and its thickness will directly affect the current and voltage output of the device (Fig. 5b). The MEL with the thickness of 2 mm can only deliver the current output of 0.99 μA and

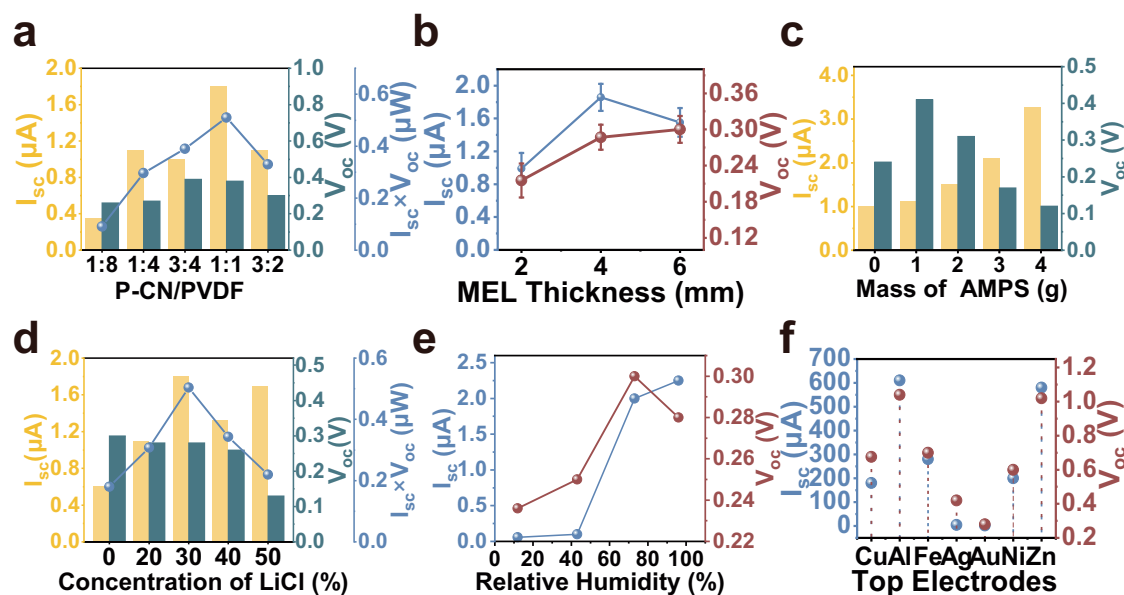


Fig. 5 | Factors affecting the electrical output performance of MEG and application outlook. a Influence of PCN/PVDF-HFP ratio on device performance. **b** Influence of MEL thickness on device performance. (Error bars are standard deviations and each contains three samples.) **c** Influence of AMPS addition on

device performance. **d** Influence of LiCl addition on device performance. **e** Influence of humidity on device performance. **f** Performance graphs of different metallic materials as top electrodes. The source data are available in the “Data availability” section.

the voltage output of 0.21 V due to the small number of ions contained in it. The MEL with a thickness of 4 and 6 mm can both produce the voltage output of ~ 0.3 V and the current output of 1.8 μA and 1.5 μA , respectively. Due to the fact that the excessively thick MEL increases the resistance of the ions to migrate, 4 mm is the optimal thickness of MEL. As shown in Fig. 5c, AMPS donates hydrogen ions in the MEL, and its addition amount has a great influence on the electrical output. The current output of the device increases with the addition of AMPS, which is due to the dissociation of more hydrogen ions to participate in the ion transport to enhance the current output of the device. The voltage increases first and then decreases with the addition of AMPS, which is due to the weakening of the Debye shielding effect in the nanopore and the decrease of the device resistance. LiCl acts as moisture adsorption sites in the hygroscopic MEL (Fig. 5d), which can effectively improve the moisture-trapping ability of the device. Therefore, moderately increasing the amount of LiCl is beneficial to improving the electrical output of the device. However, when the content of LiCl solution exceeds 30 wt%, too many free ions cause the Debye length to drop sharply, which impedes the spatial separation of anions and cations, and reduces the electrical output performance.

As a moisture-based power generation device, the effect of humidity on the device is significant (Fig. 5e). Under high humidity, the high hygroscopicity of the device ensures effective ion dissociation and provides a large electrical output. However, at high humidity, supersaturated moisture absorption leads to a decrease in the internal resistance of the device, which in turn leads to a decrease in voltage output and an enhancement in current output. Even under low humidity, the excellent hygroscopicity of the MEL can provide the voltage output slightly lower than that under high humidity, but the current output is reduced due to fewer dissociated hydrogen ions. Interestingly, the ambient humidity also affects the photocatalytic effect of the device (Supplementary Fig. 15). The photocatalytic effect will increase with the increase of humidity, that is, more dissociated hydrogen ions will promote the photocatalytic process. Since the addition of LiCl is achieved by immersing the MEL in the salt solution of the corresponding concentration, the immersion time will also affect the hygroscopicity of the device (Supplementary Fig. 16). MELs are tested for moisture absorption using three immersion times (12 h, 24 h,

48 h). The results show that the MELs treated for 12 h, 24 h, and 48 h have mass change ratios of about 97%, 149%, and 137% respectively after absorbing moisture. Too long treatment time will change the internal skeleton structure of the MEL and reduce the moisture adsorption sites, thus weaken the moisture absorption of the MEL. In addition, we tested the repeatability and durability of MEG, and tested the voltage (Supplementary Fig. 17) and current (Supplementary Fig. 18) responses of MEG under multiple light cycles. The experimental results show that the device can maintain a stable response under multiple light cycles with good durability. At the same time, using active electrodes to replace the Au inert electrode can bring the device an electrical output of up to 600 μW ($V_{oc} \times I_{sc}$), which is also higher than most reported MEGs (active electrodes) (Fig. 5f and Supplementary Table 1).

Supplementary Fig. 19 shows the schematic diagram of the device's day and night cycle power generation. Through reasonable modification and regulation of the material, the device's power generation mode can be switched between night and day. That is to say, in the absence of sunlight at night, MEG can use the ion concentration gradient inside the device to continuously generate electricity. Due to the diffusion of ions, the concentration gradient inside the device will gradually tend to equilibrium. After reaching equilibrium, when there is sunlight during the day, the device consumes the already balanced hydrogen ions through the photocatalytic effect, thereby rebuilding the ion concentration gradient inside the device and restoring the life of the device. Therefore, the device can theoretically achieve continuous power generation in a day and night cycle. More importantly, the device has the advantages of ultra-long power generation time, green and environmental protection, good adaptability to harsh environments (Supplementary Figs. 20 and 21), and multifunctional integration (dehumidification-power generation-hydrogen production), which has broad application prospects in small self-powered systems and smart wearables.

Discussion

In this work, we explored the positive role of photocatalytic effect in improving the lifetime of hydrovoltaic energy devices. We demonstrate a strategy to restore the power generation performance by using

light to rebuild the ion concentration gradient inside the hydrovoltaic device after the hydrovoltaic power generation performance decays. This strategy has the great advantages of being green, environmentally friendly, and sustainable. The V_{OC} and I_{SC} of the pure hydrovoltaic device can reach 0.28 V and 1.8 μ A, and the device can output external current for more than 600 h after short-term illumination. In addition, the device can spontaneously absorb moisture, produce hydrogen, and generate electricity in a light-humidity coupling environment. Its multifunctional integration characteristics can realize highly efficient energy saving and emission reduction. In general, this work has opened up an idea for solving the life problem of MEGs, provided a scientific explanation of the photocatalytic enhancement on the hydrovoltaic effect, and deepened the understanding of the ion transport behavior in nanopores under humid environments. However, the current work still has shortcomings. Due to the continuous consumption of hydrogen ions, the effect of improving the device lifetime under repeated illumination gradually weakens. In the future, it is recommended to simultaneously introduce a photocatalytic oxygen production reaction near the top electrode to restore the hydrogen ions at the top electrode, so as to further enhance the positive effect of photocatalysis on improving the lifetime of hydrovoltaic devices.

Methods

Materials preparation

Unless otherwise noted, all of the commercial reagents were used as received. Melamine (>98.0%, Sigma-Aldrich), chlorophyllin sodium copper salt (Chl, Aladdin), polyvinylidene fluoride-hexafluoropropylene (PVDF-HFP, Kynar 2801, Elf Atochem), tetrahydro-furan (THF, Purity (GC) \geq 99.5%, Macklin), acrylamide (AAM, Macklin), N,N'-methylene bisacrylamide (MBAA, Sigma-Aldrich), 2-acrylamido-2-methylpropane sulfonic acid (AMPS, Sigma-Aldrich), lithium chloride (LiCl, Sigma-Aldrich), 2-hydroxy-4'-(2-hydroxyethoxy)-2-methylpropiophenone (Irgacure 2959, Aladdin), sodium dodecyl benzene sulfonate (SDBS, Sigma-Aldrich), Multiwalled carbon nanotubes (MWCNTs, >95.0 wt%, Times-nano Co., Ltd.).

Preparation and modification of carbon nitride (CN)

Pristine graphitic phase carbon nitride was prepared by chemical vapor deposition (CVD) technique. The quartz boat containing 4 g of melamine was placed in a tube furnace, the tube was pumped to vacuum and then nitrogen was continuously introduced to atmospheric pressure. Heating was carried out at a rate of 10 K/min, and the temperature was kept at 773 K for 4 h to ensure that the material could be fully polymerized, and the yellowish graphite-phase carbon nitride powder could be obtained after the tube furnace naturally cooled down to room temperature. The CN powders were modified by impregnation treatment. Chl was used to prepare solutions of different concentrations (20, 30, 40, 50 mg/L), and 1 g of CN was dispersed in the solution and stirred in a 50 °C-water bath for 12 h. Wetted modified CN blocks were obtained by centrifugation as well as washing twice with anhydrous ethanol. After the modified CN blocks were dried in dryness box, these were ground with the grinding mortar to obtain photosensitized carbon nitride (P-CN) powders.

Preparation of moisture-enabled electricity generation layer (MEL)

A total of 7.71 g of AAM, 25 mg of MBAA, 2 g of AMPS and 30 mg of Irgacure 2959 were dissolved in 50 mL of deionized water and stirred for 30 min at room temperature to dissolve completely. The solution was added dropwise to a customized polytetrafluoroethylene (PTFE) mold and reacted under UV light for 15 min to make complete cross-linking. Afterwards, the gels were treated with freeze drying

technology for 6 h to obtain dry gels with nanopores. The dried gels were immersed in 30 wt% LiCl solution for 24 h to obtain the MEL.

Preparation of photocatalytic layer (PCL)

One g of PVDF-HFP, 11 g of THF and 1 g of deionized water were added into a sealed container and stirred at 500 r/min for 1 h in a 60 °C water bath. Then 1 g of P-CN was added, and stirring was continued for 2 h with the same parameters in a sealed state. The dispersion was uniformly scraped onto a clean glass plate, and allowed to stand at room temperature for 1 h to evaporate and dry to obtain the P-CN.

Fabrication of top electrode

The vacuum coating equipment (Leica EM ACE 200) was used to produce the top electrode by spraying 50 nm thick gold on the PET film and using laser cutting technology to evenly cut holes in the PET.

Fabrication of bottom electrode

One g of MWCNTs was added to 40 mL of deionized water and dispersed by ultrasonication for 45 min, then 1 g of SDBS and 10 mL of PEDOT: PSS were added to the dispersed solution and stirred in a water bath at 70 °C for 2 h to obtain the bottom electrode dispersion. The dispersion was evenly sprayed on the back of the PCL by spraying, and dried in a vacuum drying box. After three cycles, the bottom electrode was obtained.

Electrical output measurement

The device output V_{OC} , I_{SC} were recorded and scanned by semiconductor parameter analyzer (Keithley 4200 A-SCS). Impedance curves of the devices were recorded using a CHI electrochemical analyzer (CHI760E, CH Instruments, Inc, US).

Characterization methods

MEL and PCL morphology were recorded by scanning electron microscope (SEM) (Thermo Scientific Apreo 2C, US). Characterization of the crystalline phases of CN and P-CN by X-ray diffractometer (XRD) (PANalytical Empyrean Series2X, UK). Functional groups of CN and P-CN were recorded by Fourier transform infrared spectrometer (FTIR) (Thermo Scientific Nicolet iS50, US). Analysis of surface elements and functional groups of CN and P-CN by X-ray photoelectron spectroscopy (XPS) (Thermo Scientific K-Alpha, US). The zeta potential of P-CN was measured by zeta potential tester (Malvern Panalytical ZEN3600, UK). Ultraviolet-visible diffuse reflectance spectroscopy (UV-Vis DRS) (Shimadzu UV-3600, Japan) was used to measure the absorbance, band structure and transmittance of CN, P-CN and PCL as well as the transmittance of MEL. The free radicals generated during the photocatalytic process were characterized by electron paramagnetic resonance (EPR) (Bruker EMXplus-6/1, Germany). The fluorescence spectra of CN and P-CN were recorded by transient fluorescence spectrometer (PL) (Edinburgh FLS1000, UK). All-glass automatic on-line trace gas analysis system (Perfectlight Labsolar-6A, CN) was used to record the amount of hydrogen generated by the device during illumination.

Data availability

The source data used in this study are available in the Zenodo database under accession code [<https://doi.org/10.5281/zenodo.14173160>].

References

1. Yang, S. et al. Green moisture-electric generator based on supramolecular hydrogel with tens of milliamp electricity toward practical applications. *Nat. Commun.* **15**, 3329 (2024).
2. Liu, C. et al. Unveil the triple roles of water molecule on power generation of MXene derived TiO₂ based moisture electric generator. *Adv. Energy Mater.* **14**, 2400590 (2024).

3. Xu, J. et al. Sustainable moisture energy. *Nat. Rev. Mater.* **9**, 722–737 (2024).
4. Shen, D. et al. Moisture-enabled electricity generation: from physics and materials to self-powered applications. *Adv. Mater.* **32**, 2003722 (2020).
5. Yang, S. et al. Ionic hydrogel for efficient and scalable moisture-electric generation. *Adv. Mater. Process.* **34**, 2200693 (2022).
6. Shen, D. et al. Self-powered wearable electronics based on moisture-enabled electricity generation. *Adv. Mater.* **30**, 1705925 (2018).
7. Liang, Y. et al. Electric power generation via asymmetric moisturizing of graphene oxide for flexible, printable and portable electronics. *Energy Environ. Sci.* **11**, 1730–1735 (2018).
8. Yang, C., Huang, Y., Cheng, H., Jiang, L. & Qu, L. J. A. M. Rollable, stretchable, and reconfigurable graphene hygroelectric generators. *Adv. Mater.* **31**, 1805705 (2019).
9. Shao, B. et al. Electricity generation from phase transitions between liquid and gaseous water. *Adv. Energy Mater.* **13**, 2204091 (2023).
10. Tan, J. et al. Harvesting energy from atmospheric water: grand challenges in continuous electricity generation. *Adv. Mater. Process.* **36**, 2211165 (2024).
11. Wang, H. et al. Moisture adsorption-desorption full cycle power generation. *Nat. Commun.* **13**, 2524 (2022).
12. Sun, Z. et al. Weavable yarn-shaped moisture-induced electric generator. *Nano Energy* **116**, 108748 (2023).
13. He, W. et al. Textile-based moisture power generator with dual asymmetric structure and high flexibility for wearable applications. *Nano Energy* **95**, 107017 (2022).
14. Mo, J. et al. Sulfated cellulose nanofibrils-based hydrogel moist-electric generator for energy harvesting. *Chem. Eng. J.* **491**, 152055 (2024).
15. Tan, J. et al. Self-sustained electricity generator driven by the compatible integration of ambient moisture adsorption and evaporation. *Nat. Commun.* **13**, 3643 (2022).
16. Li, P. et al. Multistage coupling water-enabled electric generator with customizable energy output. *Nat. Commun.* **14**, 5702 (2023).
17. Zhao, K. et al. Moisture-driven energy generation by vertically structured polymer aerogel on water-collecting gel. *Nano Energy* **126**, 109645 (2024).
18. Long, Y. et al. Moisture-induced autonomous surface potential oscillations for energy harvesting. *Nat. Commun.* **12**, 5287 (2021).
19. Liu, X. et al. Power generation from ambient humidity using protein nanowires. *Nature* **578**, 550–554 (2020).
20. Liu, J. et al. Moisture-enabled hydrovoltaic power generation with milk protein nanofibrils. *Nano Energy* **102**, 107709 (2022).
21. Zhao, F., Cheng, H., Zhang, Z., Jiang, L. & Qu, L. J. A. M. Direct power generation from a graphene oxide film under moisture. *Adv. Mater.* **27**, 4351–4357 (2015).
22. Zhao, F. et al. Highly efficient moisture-enabled electricity generation from graphene oxide frameworks. *Energy Environ. Sci.* **9**, 912–916 (2016).
23. Zhu, R. et al. Boosting moisture induced electricity generation from graphene oxide through engineering oxygen-based functional groups. *Nano Energy* **94**, 106942 (2022).
24. Xu, T. et al. An efficient polymer moist-electric generator. *Energy Environ. Sci.* **12**, 972–978 (2019).
25. Zhang, J., Zhuang, J., Lei, L. & Hou, Y. Rapid preparation of a self-adhesive PAA ionic hydrogel using lignin sulfonate–Al³⁺ composite systems for flexible moisture-electric generators. *J. Mater. Chem. A* **11**, 3546–3555 (2023).
26. Lyu, Q. et al. Moist-induced electricity generation by electrospun cellulose acetate membranes with optimized porous structures. *ACS Appl. Mater.* **12**, 57373–57381 (2020).
27. Chen, L. et al. Nanocellulose-based functional materials for advanced energy and sensor applications. *Nano Res.* **15**, 7432–7452 (2022).
28. Zhong, H., Wang, S., Wang, Z. & Jiang, J. Asymmetric self-powered cellulose-based aerogel for moisture-electricity generation and humidity sensing. *Chem. Eng. J.* **486**, 150203 (2024).
29. Lu, X. et al. Hierarchically porous fiber-based nanofluidic diode as an efficient multimode hygroelectric generator. *Adv. Energy Mater.* **12**, 2202634 (2022).
30. Yao, Y. et al. Patterned coating of ionic diode arrays toward flexible moist-electric generators to power wireless sensor nodes. *Adv. Funct. Mater.* **34**, 2311465 (2024).
31. Yang, W. et al. Quaternized silk nanofibrils for electricity generation from moisture and ion rectification. *ACS Nano* **14**, 10600–10607 (2020).
32. Fu, C. et al. A long life moisture-enabled electric generator based on ionic diode rectification and electrode chemistry regulation. *Adv. Sci.* **11**, e2305530 (2024).
33. Lu, W. et al. Anion-cation heterostructured hydrogels for all-weather responsive electricity and water harvesting from atmospheric air. *Nano Energy* **104**, 107892 (2022).
34. Lu, J., Xu, B., Huang, J., Liu, X. & Fu, H. Charge transfer and ion occupation induced ultra-durable and all-weather energy generation from ambient air for over 200 days. *Adv. Funct. Mater.* **34**, 2406901 (2024).
35. Lu, H. et al. Tailoring the desorption behavior of hygroscopic gels for atmospheric water harvesting in arid climates. *Adv. Mater.* **34**, 2205344 (2022).
36. Li, T. et al. Simultaneous atmospheric water production and 24-hour power generation enabled by moisture-induced energy harvesting. *Nat. Commun.* **13**, 6771 (2022).
37. Huang, Y. et al. All-region-applicable, continuous power supply of graphene oxide composite. *Energy Environ. Sci.* **12**, 1848–1856 (2019).
38. Wang, H. et al. Bilayer of polyelectrolyte films for spontaneous power generation in air up to an integrated 1,000 V output. *Nat. Nanotechnol.* **16**, 811–819 (2021).
39. Wang, X. et al. Hydrovoltaic technology: from mechanism to applications. *Chem. Soc. Rev.* **51**, 4902–4927 (2022).
40. Zhang, Y. et al. Sustainable power generation for at least one month from ambient humidity using unique nanofluidic diode. *Nat. Commun.* **13**, 3484 (2022).
41. Yang, L. et al. A hybrid artificial photocatalysis system splits atmospheric water for simultaneous dehumidification and power generation. *Adv. Mater. Process.* **31**, 1902963 (2019).
42. Yang, L. et al. Solar-driven gas-phase moisture to hydrogen with zero bias. *ACS Nano* **15**, 19119–19127 (2021).
43. Yang, L. et al. Energy harvesting from atmospheric humidity by a hydrogel-integrated ferroelectric-semiconductor system. *Joule* **4**, 176–188 (2020).
44. Zhang, Y., Nandakumar, D. K. & Tan, S. C. J. J. Digestion of ambient humidity for energy generation. *Joule* **4**, 2532–2536 (2020).
45. Zhang, H. et al. High-performance, highly stretchable, flexible moist-electric generators via molecular engineering of hydrogels. *Adv. Mater.* **35**, 2300398 (2023).
46. Wang, L. et al. Preparation of Cu modified g-C₃N₄ nanorod bundles for efficiently photocatalytic CO₂ reduction. *J. Colloid Interface Sci.* **622**, 336–346 (2022).
47. Xiao, K. et al. Artificial light-driven ion pump for photoelectric energy conversion. *Nat. Commun.* **10**, 74 (2019).
48. Bhojar, T., Vidyasagar, D. & Umare, S. S. Chlorophyllin sensitized carbon nitride scaffolds for photocatalytic application. *Mater. Today Commun.* **24**, 101119 (2020).
49. Reddy, K. R. et al. Polymeric graphitic carbon nitride (g-C₃N₄)-based semiconducting nanostructured materials: synthesis methods, properties and photocatalytic applications. *J. Environ. Manag.* **238**, 25–40 (2019).

50. Fujishima, A. & Honda, K. Electrochemical photolysis of water at a semiconductor electrode. *Nature* **238**, 37–38 (1972).

Acknowledgements

The authors acknowledge the financial support from the Natural Science Foundation of Sichuan Province (Nos. 2023NSFSC0981, 2023NSFSC1988) and the Fundamental Research Funds for the Central Universities of China (Grant Nos. SWJTU 2682024CG012, 2682023QZ004, 2682023ZTPY001, 2682023KJ012, 2682022KJ017). This work was completed at the Research Center for Ultra-precision Surface Manufacturing, Southwest Jiatong University. The authors would like to thank Shiyanjia Lab (www.shiyanjia.com) for technical Support. The authors would like to thank ceshigo (www.ceshigo.com) for the SEM analysis. The authors would like to thank eceshi (www.eceshi.com) for the HER test.

Author contributions

T.Y. and P.D. provided the idea for the article. P.D. designed experiments and completed original draft. T.Y. revised and guided the article. C.W. and Y.H. analyzed the material structure. C.F. and X.L. completed the characterization of photocatalytic materials. Y.Z. and Y.Y. analyzed data and discussed the results. T.Y., L.C., L.Q. and Q.C.H. provided funding support.

Competing interests

The authors declare no competing interests.

Additional information

Supplementary information The online version contains supplementary material available at <https://doi.org/10.1038/s41467-024-55516-z>.

Correspondence and requests for materials should be addressed to Tingting Yang.

Peer review information *Nature Communications* thanks Tingxian Li and the other, anonymous, reviewer(s) for their contribution to the peer review of this work. A peer review file is available.

Reprints and permissions information is available at <http://www.nature.com/reprints>

Publisher's note Springer Nature remains neutral with regard to jurisdictional claims in published maps and institutional affiliations.

Open Access This article is licensed under a Creative Commons Attribution-NonCommercial-NoDerivatives 4.0 International License, which permits any non-commercial use, sharing, distribution and reproduction in any medium or format, as long as you give appropriate credit to the original author(s) and the source, provide a link to the Creative Commons licence, and indicate if you modified the licensed material. You do not have permission under this licence to share adapted material derived from this article or parts of it. The images or other third party material in this article are included in the article's Creative Commons licence, unless indicated otherwise in a credit line to the material. If material is not included in the article's Creative Commons licence and your intended use is not permitted by statutory regulation or exceeds the permitted use, you will need to obtain permission directly from the copyright holder. To view a copy of this licence, visit <http://creativecommons.org/licenses/by-nc-nd/4.0/>.

© The Author(s) 2024